

See discussions, stats, and author profiles for this publication at: <https://www.researchgate.net/publication/309604530>

An analytical model for electrostatic adhesive dynamics on dielectric substrates

Article in *Journal of Adhesion Science and Technology* · October 2016

DOI: 10.1080/01694243.2016.1249689

CITATIONS

22

READS

856

3 authors, including:



[Rui Chen](#)

Chongqing University

30 PUBLICATIONS 382 CITATIONS

SEE PROFILE



An analytical model for electrostatic adhesive dynamics on dielectric substrates

Rui Chen, Yao Huang & Qian Tang

To cite this article: Rui Chen, Yao Huang & Qian Tang (2017) An analytical model for electrostatic adhesive dynamics on dielectric substrates, Journal of Adhesion Science and Technology, 31:11, 1229-1250, DOI: [10.1080/01694243.2016.1249689](https://doi.org/10.1080/01694243.2016.1249689)

To link to this article: <http://dx.doi.org/10.1080/01694243.2016.1249689>



Published online: 31 Oct 2016.



Submit your article to this journal [↗](#)



Article views: 32



View related articles [↗](#)



View Crossmark data [↗](#)



Citing articles: 2 View citing articles [↗](#)



An analytical model for electrostatic adhesive dynamics on dielectric substrates

Rui Chen, Yao Huang and Qian Tang

State Key Laboratory of Mechanical Transmissions, Chongqing University, Chongqing, People's Republic of China

ABSTRACT

For electrostatic adhesion on a dielectric material, the electrostatic adhesion force gradually increases to a steady value after the voltage exerted onto the interdigital electrodes. However, little has been addressed to reveal governing mechanisms behind this dynamic phenomenon. In this paper, a theoretical model is presented for analysis of the dynamic properties of electrostatic adhesion on dielectric materials. Firstly, the electric field was derived by solving the Laplace equation of the electrical potential for each sub-area using general solution and boundary conditions. Then, the electrostatic adhesion force was obtained using the Maxwell stress tensor formulation. Finally, the dynamic properties of the electric field and electrostatic adhesion force were assessed by evaluating the transient response of the field and force under a step in applied voltages. Experimental studies for verification were conducted by evaluating the adhesion performance of an electrode panel on three different substrate plates: glass, wood and Polyvinylidene Fluoride (PVDF). Results from these experiments are highly consistent with the theoretical model. The overall results of this paper provide theoretical guidelines for systematic optimization of electrostatic adhesion technology in various application scenarios, such as electrostatic chucks, electrostatic suspension systems and electroadhesive wall-climbing robots.

ARTICLE HISTORY

Received 19 July 2016
Revised 11 October 2016
Accepted 12 October 2016

KEYWORDS

Electrostatic adhesion force; electric field; interdigital electrodes; dynamic properties

1. Introduction

Electrostatic adhesion is widely exploited in the manufacture and processing of many contemporary electrical devices,[1] most prominently in the areas of laser printing, dust cleaning and cathode ray tube technology used for televisions and computer displays. In recent years, considerable research has been devoted to the development of various industrial-use electrostatic adhesion devices. The electrostatic chuck used for wafer handling or workpiece fixing in semiconductor manufacture is one of the most important results of this research.[2,3] Such an electrostatic chuck possesses several advantages compared with a mechanical holding system. Since the electrostatic force is uniformly distributed over

the object's surface, an electrostatic chuck can hold the object flat, avoiding the common problem of structure deformation in the process of mechanical manipulation. Furthermore, an electrostatic chuck can transport a wafer faster than a mechanical gripper, and thus improves production yields, while a mechanical gripper requires low speed movement to avoid particle generation. Electrostatic suspension systems are another effective application of the principles of electrostatic force.[4–6] These noncontact holding systems can not only avoid structure deformation of the material, but also circumvent surface contamination and particle generation. Electrostatic adhesion forces have also been exploited for biological research. Dielectrophoresis is an important alternating current (AC) electrokinetic technique currently being used for analysis and separation of biological particles, such as cells, bacteria and viruses.[7–10] Polarizable particles move towards or away from regions of strong field by dielectrophoresis force. The force levitates different particles to different heights producing a vertical separation. Electrostatic adhesion, also known as electrically controllable adhesion technology, has also recently been applied to wall-climbing robots.[11–13] This works by inducing electrostatic charges on a wall surface using a power supply connected to compliant pads placed on the moving robot. Using this technology, various wall-climbing robots have been demonstrated, including robots with feet and tracks. Although the adhesion forces generated per unit area by electro-adhesion is relatively weak compared to other methods, such as magnetic methods, suction methods and so on, and it may fail in high-moisture environments, electro-adhesion is a promising approach enabling robots to have several advantages, including being adaptable to various wall surfaces, having simpler and lighter structures, being quiet and fast in locomotion and ultra-low energy consumption (usually microwatts).[14]

While practical applications of the electrostatic adhesion technique have been widely investigated in recent years, the technique is far from mature and reliable, especially for adhesion on dielectric materials. One of the key problems is the fact that the response time may be too long to achieve stable adhesion on dielectric materials, which may result in adhesion instability or failure and therefore limits its practical use. This problem stems from the fact that the mechanism of electrostatic adhesion on conductive materials and dielectric materials are different. For a conductive material, electrons are free to move throughout the conductor allowing them to migrate under the positive electrodes and generate electron holes under the negative electrodes. This causes the adhesion system to act as a set of capacitors where the plates of the capacitor are attracted to each other. Since free charges inside a conductor can move freely, these charges will uniformly distribute on the surface facing the electrode immediately after voltage is applied to electrodes. However, in the case of a dielectric material, charge collection mainly originates from polarization, which can usually not occur instantaneously. Hence, a dynamic relation, which includes a time-varying function, exists between the applied electrode voltages and electrostatic adhesion force due to the resistivity of the dielectric or the delayed polarization.

Considerable experimental work has been done to evaluate the time-varying properties of the electrostatic adhesion force generated on dielectric materials. Researchers at NASA's Langley Research Center experimentally measured the time for the build-up of adhesion force in 1968.[15] The test results indicated that the amount of time required for the force to build-up depends on the relative permittivity and the resistivity of the materials. The electrostatic forces vs. chucking time were obtained through experiments of an electrostatic chuck for quartz, sapphire, and glass-ceramic dielectrics by Kalkowski et al. [16] There are

major differences in the functional variation of force with time between these materials, and a strong increase is observed for the glass-ceramic material. Jong up Jeon et al. [4] established an electrostatic suspension system for glass plate handling. The suspension initial time was measured to analyse the dynamic stability of the suspension system. A time-delay phenomenon was noticed since the charge accumulation was progressing continuously during suspension before reaching a steady state. Zhang et al. [17,18] studied the dynamic property of an electrostatic gripper for handling of fabric materials. Different adhesion times, varying from several milliseconds to tens of seconds, were found for handling different fabric materials. Akio Yamamoto et al. [11] evaluated the electrostatic adhesion on a glass wall for a wall-climbing robot design. The holding force was measured at different time intervals after a voltage was exerted. The results show that the electrostatic adhesion force does not immediately occur but gradually grows with a time constant of about 1000 s. Guo et al. [19] investigated the relationship between interfacial electroadhesive force and surface texture. A dynamic changing of the obtainable electroadhesive forces is presented. This dynamic electrostatic attraction phenomenon can be seen in the pad charging phase after turning on the voltage. Despite the fact that dynamic properties of the electrostatic adhesion on dielectric materials have been noticed and experimentally studied, literature on the theoretical analysis of the dynamic properties of the electric field and the electrostatic adhesion force remains scarce. Liu et al. [20] proposed a model to analyse the dynamic electric field and electrostatic adhesion force produced by interdigital electrodes, and the time histories of the electrostatic adhesion force exerted on a glass pane was obtained.

In this paper an analytical model is presented for theoretical analysis of the dynamic properties of electrostatic adhesion. A typical adhesion system consisting of an interdigital electrode panel and a substrate plate positioned below the electrode panel is introduced. The electric fields are firstly derived by solving the Laplace equation of the potential distribution in the adhesion system with boundary conditions taken into account. Then, the electrostatic adhesion force is calculated by the Maxwell stress tensor formulation. Finally, the dynamic properties of the electric field and electrostatic adhesion force are assessed by evaluating the transient response of the field and force under a step in applied voltages. Experiments were carried out to evaluate the adhesion performance of the electrode panel on three different substrate plates: glass, wood and PVDF, and the experimental results verify the correctness of the theoretical model.

2. Theoretical derivation

2.1. Physical model

The structure layout of the interdigital electrode arrays and the sectional view of the adhesion model are shown in Figure 1. The interdigital electrode arrays are comprised of two comb electrodes treated as the positive and negative electrode with applied voltages $V_p(t)$ and $V_n(t)$, respectively. The overlapping length of the positive and negative electrode is L , the width of electrodes is $2w$, and p denotes the space between the adjacent positive and negative electrodes. The upper and lower surface of the electrodes are covered with insulating dielectrics as the insulating cover layer and the insulating base layer with respective thickness of d_1 and d_2 , and permittivity and volume conductivity of ϵ_p and σ_p . Given the roughness of the substrate plate, a simplified thin air layer with a thickness of d_3 is introduced

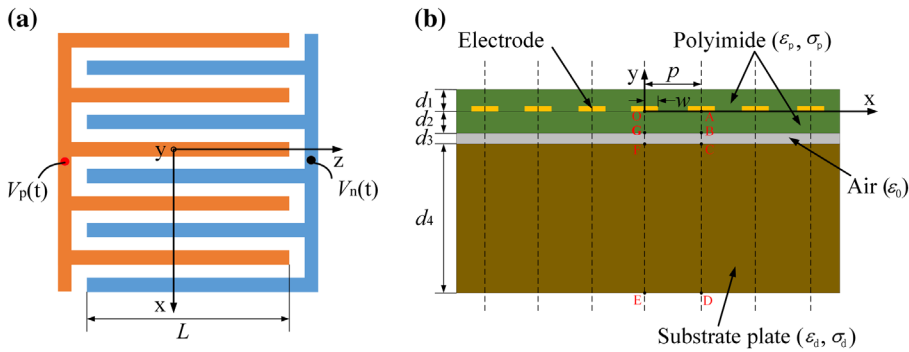


Figure 1. (a) Layout of interdigital electrode arrays; (b) Cross section of the adhesion model.

between the electrode panel and the substrate plate. The permittivity, volume conductivity and thickness of the dielectric plate are ϵ_d , σ_d and d_4 , respectively.

2.2. Basic equations and assumptions

Assuming that the rate of current change in the model is negligible (and thus the magnetic effect is efficiently non-existent), Maxwell's equations can be written in the form [21]:

$$\mathbf{E} = -\nabla\phi, \quad (1)$$

$$\nabla \cdot \mathbf{D} = \rho, \quad (2)$$

$$\nabla \cdot \mathbf{J} + \frac{\partial \rho}{\partial t} = 0, \quad (3)$$

where \mathbf{E} is the electric field, \mathbf{D} is the displacement vector, ρ is the free charge density, and \mathbf{J} is the conduction current. For a linear homogeneous dielectric with permittivity ϵ and conductivity σ , $\mathbf{D} = \epsilon\mathbf{E}$ and $\mathbf{J} = \sigma\mathbf{E}$.

Simplifications and assumptions can be made when considering the special structure of the interdigital electrode arrays. Firstly, since the electric field is mainly generated between the adjacent positive and negative electrodes, the interdigital electrode arrays can be simplified to a series of strip electrodes by ignoring the effect of the roots of comb electrodes. Secondly, the edge effect of the electric field along the length direction can be neglected due to the much larger length of the electrode compared to its width as well as the thickness of the air layer. In addition, the uniform distribution of the electric field in the longitudinal direction provides basis to reduce the original three-dimensional electrostatic adhesion problem into a two-dimensional problem. Finally, because of the presence of the periodic electrode structure, a single period is chosen as the research object. As shown in Figure 1, the electrode structure is even symmetric along the dashed line. Therefore, the area OADE is regarded as the research object to sufficiently extend the problem to the entire space.

There are three different dielectrics in the area OADE, and are all assumed to be linearly homogeneous. To handle the discontinuous electric fields in the dielectric interfaces GB and FC, the area OADE is further divided into three homogeneous sub-areas: OABG, GBCF and

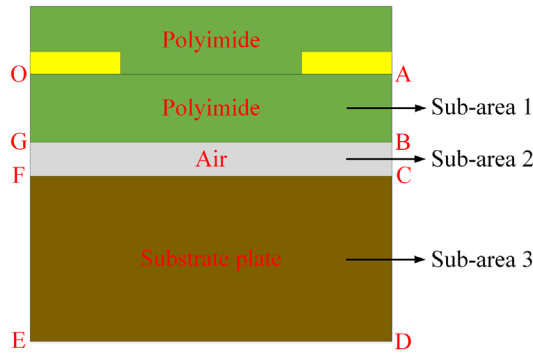


Figure 2. Three sub-areas of the research area including polyimide film, air layer and substrate plate.

FCDE, which will be denoted as sub-area 1, sub-area 2 and sub-area 3 as shown in Figure 2 in the following discussion. The potential function must satisfy the Laplace equation in every sub-area, and can be written as:

$$\frac{\partial^2 \emptyset(x, y, t)}{\partial x^2} + \frac{\partial^2 \emptyset(x, y, t)}{\partial y^2} = 0, \quad (4)$$

where $\emptyset(x, y, t)$ is the time-varying spatial potential distribution function. Using the method of separation of variables,[21] the partial differential Equation (4) can be transformed into the following two ordinary differential equations:

$$\begin{cases} \frac{d^2 X(x, t)}{dx^2} + \lambda^2 X(x, t) = 0 \\ \frac{d^2 Y(y, t)}{dy^2} - \lambda^2 Y(y, t) = 0, \end{cases} \quad (5)$$

where λ is the separation constant. Two independent particular solutions $\emptyset_{\lambda=0}(x, y, t)$ and $\emptyset_{\lambda \neq 0}(x, y, t)$ can be obtained, and a general solution of $\emptyset(x, y, t)$ can be acquired by combining these two particular solutions:

$$\begin{aligned} \emptyset(x, y, t) &= \emptyset_{\lambda=0}(x, y, t) + \emptyset_{\lambda \neq 0}(x, y, t) \\ &= [A(t)x + B(t)][C(t)y + D(t)] \\ &\quad + [E(t) \sin(\lambda x) + F(t) \cos(\lambda x)][G(t) \sinh(\lambda y) + H(t) \cosh(\lambda y)], \end{aligned} \quad (6)$$

where $A(t)$, $B(t)$, $C(t)$, $D(t)$, $E(t)$, $F(t)$, $G(t)$ and $H(t)$ are time-varying undetermined coefficients. The separation constant λ and the undetermined coefficients will be determined by considering the boundary conditions in the following.

2.3. Boundary conditions

In the three sub-areas, the potential functions are bounded and symmetrical at $x = 0$ and $x = p$. Hence, the model must match Riemann boundary conditions:

$$\frac{\partial \emptyset(0, y, t)}{\partial x} = 0, \quad \frac{\partial \emptyset(p, y, t)}{\partial x} = 0 \quad - (d_2 + d_3 + d_4) \leq y \leq 0. \quad (7)$$

Since the thickness of the copper electrode is much smaller than its width, potential on the electrode is considered distributed at $y = 0$ by ignoring the thickness of the copper electrode. The potentials on the positive and negative electrodes are $V_p(t)$ and $V_n(t)$, respectively, but the potentials within the gap between the positive and negative electrodes remains unknown, leading to incomplete boundary condition of the potential distribution at $y = 0$. To simplify the calculations, first-order Taylor series expansion were used to estimate the potential in the gap between the positive and negative electrodes. Although the accuracy of estimation would be much improved by introducing higher order Taylor series expansion, some special processing would consequently be required to deal with the highly complicated calculation (details are addressed in discussion section). The boundary condition of the potential distribution at $y = 0$ can be expressed as:

$$\varnothing(x, 0, t) = \begin{cases} V_p(t) & 0 \leq x \leq w \\ \frac{V_p(t) + V_n(t)}{2} + \left[V_n(t) - V_p(t) \right] \frac{x - p/2}{p - 2w} & w < x < p - w \\ V_n(t) & p - w \leq x \leq p. \end{cases} \quad (8)$$

The potential function at $y = 0$ is piecewise smooth in the interval $0 \leq x \leq p$, which can be converted to a continuous smooth function by using the Fourier series expansion. Since the potential function is even symmetrical on the y -axis, only the cosine terms are retained in the Fourier series representation:

$$\varnothing(x, 0, t) = \frac{a_0(t)}{2} + \sum_{n=1}^{\infty} a_n(t) \cos\left(\frac{n\pi x}{p}\right) \quad 0 \leq x \leq p, \quad (9)$$

where

$$a_n(t) = \frac{2}{p} \int_0^p \varnothing(x, 0, t) \cos\left(\frac{n\pi x}{p}\right) dx \quad (n = 0, 1, 2, \dots). \quad (10)$$

Substitution of Equations (8) and (10) into Equation (9) yields the following Fourier series representation of the electric potential at the boundary $y = 0$:

$$\begin{aligned} \varnothing(x, 0, t) = & \frac{V_p(t) + V_n(t)}{2} \\ & + \frac{2[V_n(t) - V_p(t)]}{\pi^2(1 - 2w/p)} \sum_{n=1}^{\infty} \frac{1}{n^2} \left[\cos\left(n\pi - \frac{n\pi w}{p}\right) \right. \\ & \left. - \cos\left(\frac{n\pi w}{p}\right) \right] \cos\left(\frac{n\pi x}{p}\right) \quad 0 \leq x \leq p. \end{aligned} \quad (11)$$

Two boundary conditions need to be considered owing to the discontinuity of the electric fields at the interfaces of the three sub-areas. The first is the irrotational condition of the electric field, which can be expressed as [22]:

$$\begin{aligned} \mathbf{n} \times (\mathbf{E}_1 - \mathbf{E}_2) &= 0 \quad y = -d_2, \\ \mathbf{n} \times (\mathbf{E}_2 - \mathbf{E}_3) &= 0 \quad y = -(d_2 + d_3). \end{aligned} \quad (12)$$

The second is associated with the current continuity at the interfaces, which can be expressed as [17]:

$$\begin{aligned}\frac{\partial}{\partial t} \mathbf{n} \cdot (\epsilon_p \mathbf{E}_1 - \epsilon_0 \mathbf{E}_2) + \mathbf{n} \cdot (\sigma_p \mathbf{E}_1) &= 0 \quad y = -d_2, \\ \frac{\partial}{\partial t} \mathbf{n} \cdot (\epsilon_0 \mathbf{E}_2 - \epsilon_d \mathbf{E}_3) - \mathbf{n} \cdot (\sigma_d \mathbf{E}_3) &= 0 \quad y = -(d_2 + d_3),\end{aligned}\quad (13)$$

where \mathbf{n} represents the unit vector of y -axis direction, \mathbf{E}_1 , \mathbf{E}_2 and \mathbf{E}_3 represent the electric field in sub-area 1, sub-area 2 and sub-area 3, respectively.

The thickness of the substrate plate is usually much greater than that of the insulating base layer and the air layer ($d_4 \gg d_2$, $d_4 \gg d_3$). Thus, the thickness of the substrate plate can be regarded as infinity for reasonable simplification. The last boundary condition expresses that the potential decays to zero when y approaches infinity, that is:

$$\lim_{y \rightarrow -\infty} \emptyset(x, y, t) = 0. \quad (14)$$

Equations (7), (11), (12), (13) and (14) constitute a complete set of boundary conditions to solve the posed boundary value problem of spatial potential distribution.

2.4. Solution to the Laplace equation

In order to solve the potential distributions in the three sub-areas, we need to solve the Laplace equation for each region incorporating the general solution and boundary conditions. The solution to the Laplace equation for sub-area 1 is discussed first. Substituting the first Riemann-type boundary condition in Equation (7) into the partial derivative of Equation (6) with respect to x yields:

$$\begin{aligned}\frac{\partial \emptyset_1(0, y, t)}{\partial x} &= A^1(t) [C^1(t)y + D^1(t)] + \lambda E^1(t) [G^1(t) \sinh(\lambda y) + H^1(t) \cosh(\lambda y)] \\ &= 0 \quad \forall y, t \text{ and } \lambda \neq 0,\end{aligned}\quad (15)$$

where subscript 1 and superscript 1 both denote the sub-area 1. This boundary condition can be satisfied by enforcing $C^1(t) = 0$, $A^1(t)D^1(t) = 0$ and $E^1(t) = 0$. Substitution of the second Riemann-type boundary condition in Equation (7) into the partial derivative of Equation (6) with respect to x leads to:

$$\begin{aligned}\frac{\partial \emptyset_1(p, y, t)}{\partial x} &= -\lambda F^1(t) \sin(\lambda p) [G^1(t) \sinh(\lambda y) + H^1(t) \cosh(\lambda y)] \\ &= 0 \quad \forall y, t \text{ and } \lambda \neq 0.\end{aligned}\quad (16)$$

This boundary condition can be only met when $\sin(\lambda p) = 0$ for $\lambda \neq 0$ and $F^1(t) \neq 0$, which means that the separation constant:

$$\lambda = \frac{n\pi}{p} \quad n = 1, 2, \dots, \infty. \quad (17)$$

By introducing the notations $K^1(t) = B^1(t)D^1(t)$, $L^1(t) = F^1(t)G^1(t)$ and $M^1(t) = F^1(t)H^1(t)$, the solution to Laplace equation for sub-area 1 can be given as follows:

$$\emptyset_1(x, y, t) = K^1(t) + \sum_{n=1}^{\infty} \left[L_n^1(t) \sinh\left(\frac{n\pi y}{p}\right) + M_n^1(t) \cosh\left(\frac{n\pi y}{p}\right) \right] \cos\left(\frac{n\pi x}{p}\right). \quad (18)$$

Another boundary condition associated with sub-area 1 is the potential distribution on the plane $y = 0$, which has been given by Equation (11). Matching the terms in Equation (11) with Equation (18) at $y = 0$ yields the following two relationships:

$$K^1(t) = \frac{V_p(t) + V_n(t)}{2} \quad (19)$$

and

$$M_n^1(t) = \frac{2[V_n(t) - V_p(t)]}{n^2\pi^2(1 - 2w/p)} \left[\cos\left(n\pi - \frac{n\pi w}{p}\right) - \cos\left(\frac{n\pi w}{p}\right) \right]. \quad (20)$$

With respect to the solution to Laplace equation for sub-area 2, we assume a form similar to that of $\emptyset_1(x, y, t)$:

$$\emptyset_2(x, y, t) = K^2(t) + \sum_{n=1}^{\infty} \left[L_n^2(t) \sinh\left(\frac{n\pi y}{p}\right) + M_n^2(t) \cosh\left(\frac{n\pi y}{p}\right) \right] \cos\left(\frac{n\pi x}{p}\right). \quad (21)$$

In sub-area 3, a particular boundary condition expressed by Equation (14) results in a different form of potential expression as the form in sub-area 1, and it can be written as:

$$\emptyset_3(x, y, t) = K^3(t) + \sum_{n=1}^{\infty} L_n^3(t) \exp\left(\frac{n\pi y}{p}\right) \cos\left(\frac{n\pi x}{p}\right). \quad (22)$$

The eight unknown time-varying coefficients in the potential expressions of the three sub-areas can be obtained by substituting the solutions to Laplace equation for the three sub-areas into the boundary conditions at the two dielectric interfaces [Equations (12) and (13)] and incorporating the two relationships shown in Equations (19) and (20). As a workaround, Laplace transforms of the time functions is adopted to circumvent the computational difficulty created by the presence of the time derivatives of field solutions in the boundary conditions [Equation (13)]. The Laplace transforms of time domain functions are denoted by replacing the time variable t with the complex variable s . Hereto, the solutions to Laplace equation for the three sub-areas can all be solved provided we obtain the Laplace transforms of the eight unknown time-varying coefficients $K^1(s)$, $L_n^1(s)$, $M_n^1(s)$, $K^2(s)$, $L_n^2(s)$, $M_n^2(s)$, $K^3(s)$ and $L_n^3(s)$ (see Appendix 1).

2.5. Electric field and electrostatic adhesion force

Based on the solutions to Laplace equation in sub-area 1, 2, 3, each of the electric field components in the three regions can be derived from Equation (1):

$$\begin{aligned} E_{r,x}(x, y, s) &= \frac{\pi}{p} V_{\nabla}(s) \sum_{n=1}^{\infty} n\gamma(n) \sin\left(\frac{n\pi x}{p}\right) \times \frac{a_{2,x}^r(n,y)s^2 + a_{1,x}^r(n,y)s + a_{0,x}^r(n,y)}{b_2(n)s^2 + b_1(n)s + b_0(n)}, \\ E_{r,y}(x, y, s) &= -\frac{\pi}{p} V_{\nabla}(s) \sum_{n=1}^{\infty} n\gamma(n) \cos\left(\frac{n\pi x}{p}\right) \times \frac{a_{2,y}^r(n,y)s^2 + a_{1,y}^r(n,y)s + a_{0,y}^r(n,y)}{b_2(n)s^2 + b_1(n)s + b_0(n)}, \end{aligned} \quad (23)$$

where $r = 1, 2, 3$ and

$$\begin{aligned}
 a_{l,x}^1(n, y) &= a_{l,L_1}(n) \sinh\left(\frac{n\pi y}{p}\right) + b_l(n) \cosh\left(\frac{n\pi y}{p}\right), \\
 a_{l,y}^1(n, y) &= a_{l,L_1}(n) \cosh\left(\frac{n\pi y}{p}\right) + b_l(n) \sinh\left(\frac{n\pi y}{p}\right), \\
 a_{l,x}^2(n, y) &= a_{l,L_2}(n) \sinh\left(\frac{n\pi y}{p}\right) + a_{l,M_2}(n) \cosh\left(\frac{n\pi y}{p}\right), \\
 a_{l,y}^2(n, y) &= a_{l,L_2}(n) \cosh\left(\frac{n\pi y}{p}\right) + a_{l,M_2}(n) \sinh\left(\frac{n\pi y}{p}\right), \\
 a_{m,x}^3(n, y) &= a_{m,y}^3(n, y) = a_{m,L_3}(n) \exp\left(\frac{n\pi y}{p}\right), \\
 a_{0,x}^3(n, y) &= a_{0,y}^3(n, y) = 0.
 \end{aligned}$$

According to the Maxwell stress tensor formulation, the net i th force component on a dielectric medium can be calculated by integrating the Maxwell stress tensor T_{ij} over the enclosing surface S [22]:

$$F_i = \varepsilon_0 \oint_s (T_{ij} n_j) dA = \varepsilon_0 \oint_s \left[\left(E_i E_j - \frac{1}{2} \delta_{ij} E_k E_k \right) n_j \right] dA. \quad (24)$$

In addition, according to the boundary condition shown in Equation (14), the potential on the lower surface of the substrate plate will decay to zero, and therefore the electric field will decay to zero as well. This implies that only the electric field solution in sub-area 2 is required in the integration, and the electrostatic adhesion force exerted on the substrate plate of one period can be written as:

$$F = \frac{\varepsilon_0 L}{2} \int_0^p \left[E_{2,y}^2(x, y, t) - E_{2,x}^2(x, y, t) \right] dx. \quad (25)$$

The time domain electric field components required to evaluate the above expression can be obtained straightforwardly by applying the inverse Laplace transform to Equation (23).

3. Model verification and analysis

3.1. Field and force dynamics under a step voltage excitation

Since free charges inside a conductor can move freely, these charges will appear on the surface facing the electrodes nearly uniformly immediately after voltages are applied to electrodes. However, in the case of a dielectric, charge collection mainly originates from polarization, which usually does not occur instantaneously. Hence, a dynamic relation, which includes a time-varying function, exists between the applied electrode voltages and electrostatic adhesion force due to the resistivity of the dielectric or the delayed polarization.

In this work, the field and force dynamics are assessed by evaluating the transient response of the field and force under a step in applied voltages, which is similar to the actual adhesion process where the voltages exerted to the electrodes may actually behave like a step input. Let us define the step voltages as:

$$\begin{cases} V_p(t) = 0 & t \leq 0 \\ V_p(t) = V_p & t > 0 \end{cases}, \quad \begin{cases} V_n(t) = 0 & t \leq 0 \\ V_n(t) = V_n & t > 0 \end{cases}. \quad (26)$$

The Laplace transforms of these step voltages are given by $V_p(s) = V_p/s$ and $V_n(s) = V_n/s$, respectively. Equation (23) demonstrates the relationship between the input voltage $V_v(s)$ and each of the field components, which is described by an infinite series of second-order, rational transfer functions, whose denominator and numerator polynomial coefficients are functions of the summation index n . Since the transfer function completely represents a system differential equation, its poles, namely the roots of the denominator polynomials, and zeros, namely the roots of the numerator polynomials, can effectively define the system response.

Let $[p_1(n); p_2(n)]$ and $[z_{1,l}^r(n); z_{2,l}^r(n)]$ denote the poles and zeros of the second-order transfer functions in the series expansion of the field components [Equation (23)], where the subscript l ($l = x, y$) and superscript r ($r = 1, 2, 3$) refers to the axis orientation of the field component and the sub-area, respectively. The step response of the field in the time domain can be expressed in terms of the poles and zeros by applying the inverse Laplace transform to Equation (23), yielding the following field components:

$$\begin{aligned} E_{r,x}(x, y, t) &= \frac{\pi}{p} (V_p - V_n) \sum_{n=1}^{\infty} n \gamma(n) \sin\left(\frac{n\pi x}{p}\right) T_{r,x}(y, n, t), \\ E_{r,y}(x, y, t) &= \frac{\pi}{p} (V_p - V_n) \sum_{n=1}^{\infty} n \gamma(n) \cos\left(\frac{n\pi x}{p}\right) T_{r,y}(y, n, t), \end{aligned} \quad (27)$$

where the time domain function $T_{r,x}(y, n, t)$ is given by:

$$\begin{aligned} T_{r,l}(y, n, t) &= \frac{a_{2,l}^r(n, y)}{b_2(n)} \left\{ \frac{z_{1,l}^r(n) z_{2,l}^r(n)}{p_1(n) p_2(n)} \right. \\ &\quad + \frac{[z_{2,l}^r(n) - p_1(n)][z_{1,l}^r(n) - p_1(n)]}{p_1(n)[p_1(n) - p_2(n)]} \exp[p_1(n)t] \\ &\quad \left. - \frac{[z_{2,l}^r(n) - p_2(n)][z_{1,l}^r(n) - p_2(n)]}{p_2(n)[p_1(n) - p_2(n)]} \exp[p_2(n)t] \right\}, \end{aligned} \quad (28)$$

where $r = 1, 2, 3$ and $l = x, y$. Hence, the dynamic force expression can be derived by substituting $E_{2,x}(x, y, t)$ and $E_{2,y}(x, y, t)$ into Equation (25).

3.2. Experimental procedure

In order to verify the theoretical model, adhesion performances of a flexible interdigital electrode panel on three different substrate plates: glass, wood, and PVDF are evaluated.

The electrode panel shown in Figure 3 is made from a flexible etched printed circuit board process. The base of the panel is a polyimide film, 50 μm in thickness. Interdigital electrodes made from the copper film are deposited on the polyimide base, which are then covered with another polyimide film with a thickness of 50 μm . The width of the electrode and the space between neighbouring electrodes are both 1 mm. The total area of the electrode panel is 300 \times 240 mm. The relative permittivity and bulk conductivity of the three substrate plates are measured by a relative permittivity analyser and a bulk resistivity analyser, which are shown in Tables 1 and 2, respectively. The three substrate plates have a thickness (d_4) of 5 mm, while the thickness of the air layers between the electrode panel and the three substrate plates due to the influence of roughness are experimentally calibrated since they are difficult to measure directly. The results are shown in Table 3. The applied step voltages are $V_p = 1000\text{ V}$ and $V_n = -1000\text{ V}$.

Since the adhesion force between the electrode panel and the substrate are varying with time, it is a little difficult to measure the dynamic adhesion force accurately. To this point, little work has been done to measure the dynamic electrostatic adhesion force though the final stable force can be easily measured by a lot of researchers. In this paper, a measurement method has been proposed, which we named as the repeated trial weight method. We have prepared several sets of weights, from 50 g to 20 kg. We added or reduced the weights to measure the force. To be specific, we can obtain the theoretical calculated forces at some

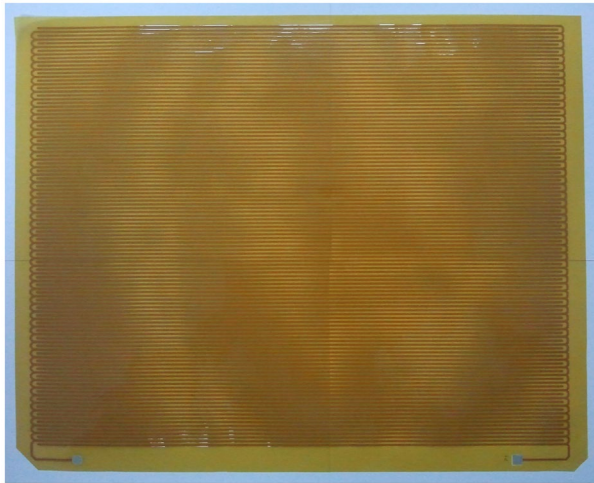


Figure 3. An electrode panel with a pair of interdigital electrodes.

Table 1. Relative permittivities of three different substrate plates.

Substrate plates	Glass	Wood	PVDF
Relative permittivities	4.1	2.8	8.4

Table 2. Bulk conductivities of three different substrate plates (S/cm).

Substrate plates	Glass	Wood	PVDF
Bulk conductivities	10^{-13}	5×10^{-14}	2×10^{-14}

Table 3. Thickness of air layers between the electrode panel and the three substrate plates (μm).

Substrate plates	Glass	Wood	PVDF
Thickness of air layers	15	20	25

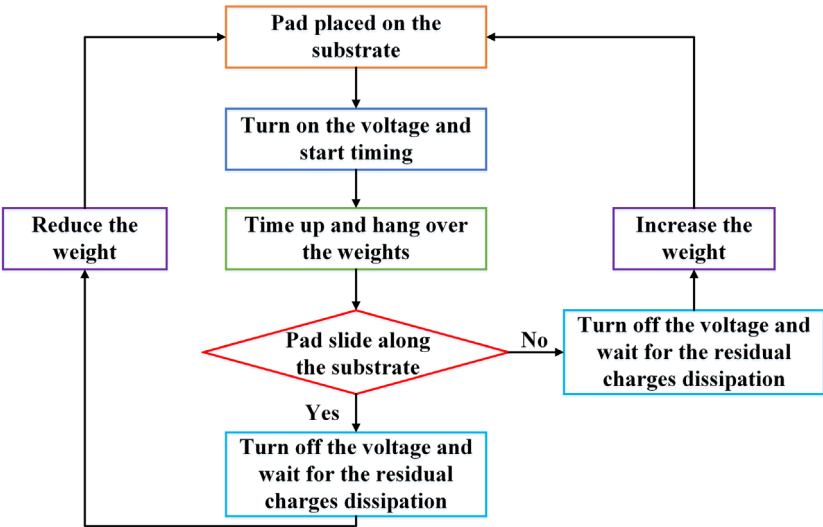


Figure 4. Measurement procedure of electrostatic adhesion force at a specific set time.

specific time (e.g. $t = 10\text{ s}$, 20 s , ...) using the proposed model firstly. Then an approximate amount of weights were hung over the hook at the specific time according to the theoretical value. If the pad slides along the substrate, we will reduce the weights in the next test. On the contrary, if the pad still adheres to the substrate firmly, we will increase the weights in the next test. Through several repeated tests, we can limit the lateral holding force in a more and more narrow interval and eventually determine the experimental force at every specific time approximately. At last, the electrostatic adhesion force is obtained indirectly by a simple conversion between the lateral force and the friction coefficient. The measurement procedure of electrostatic adhesion force at a specific set time can be seen in Figure 4, and the adhesion experiments on three different substrate plates are shown in Figure 5. The accuracy of the measurement method we used is not high enough compared with the method of using a force/torque sensor by Guo et al. [19] but it is very simple and direct for operation.

3.3. Theoretical results

Based on the expressions of electric fields in Section 2.5, the dynamic changes of electric fields were calculated and drawn by MATLAB, as shown in Figures 6–8. As seen from the figures, all electric field components tend to zero gradually as time increases, except the electric field component along the y -axis direction of the upper surface of the substrate

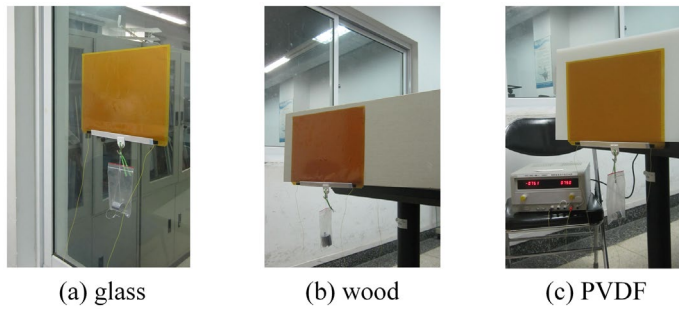


Figure 5. Adhesion experiments on three different substrate plates.

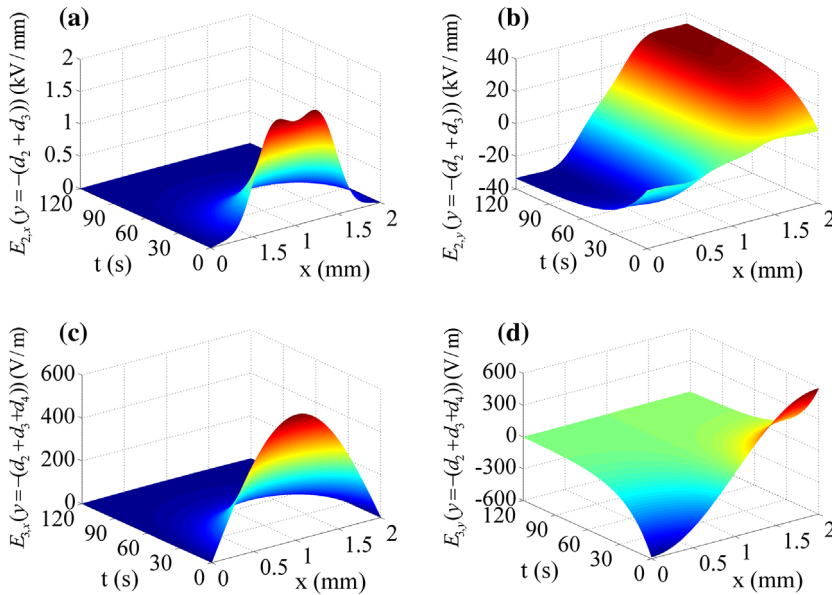


Figure 6. The step response of the electric field components as a function of time (t) and distance (x) along the boundary $y = -(d_2 + d_3)$ in region 2 [(a) and (b)] and $y = -(d_2 + d_3 + d_4)$ in region 3 [(c) and (d)] (glass plate).

plate. Moreover, the electric field component of the lower surface is far less than that of the upper surface, and this verifies the reasonability of ignoring the effect of the electric field of the lower surface.

3.4. Comparison between experimental and theoretical results

The time histories of the electrostatic adhesion forces exerted on the three substrate plates are shown in Figures 9–11, including the experimental values and the theoretical values. The experimental values are smaller than the theoretical values in the initial phase of adhesion while larger in the later phase, and this is due to the thickness variation of the air layer. The thickness of the actual air layer is larger than that of the equivalent air layer in the initial

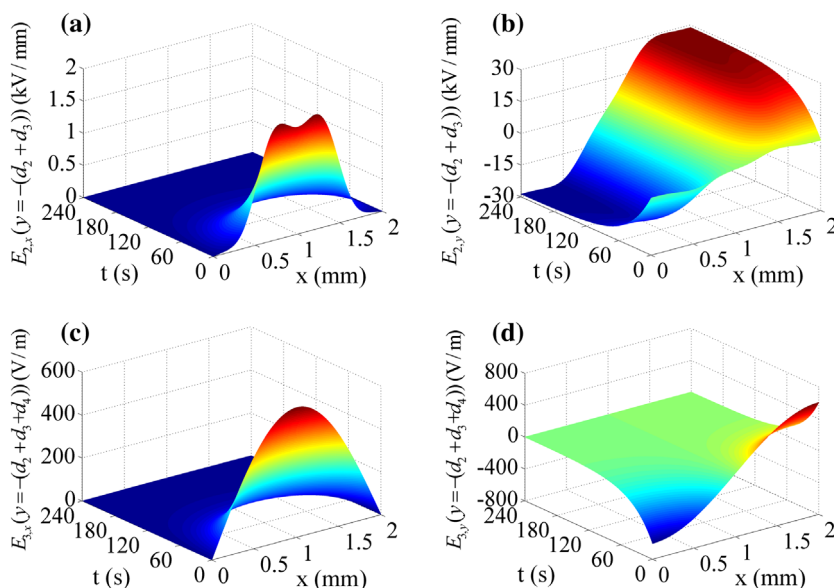


Figure 7. The step response of the electric field components as a function of time (t) and distance (x) along the boundary $y = -(d_2 + d_3)$ in region 2 [(a) and (b)] and $y = -(d_2 + d_3 + d_4)$ in region 3 [(c) and (d)] (wood plate).

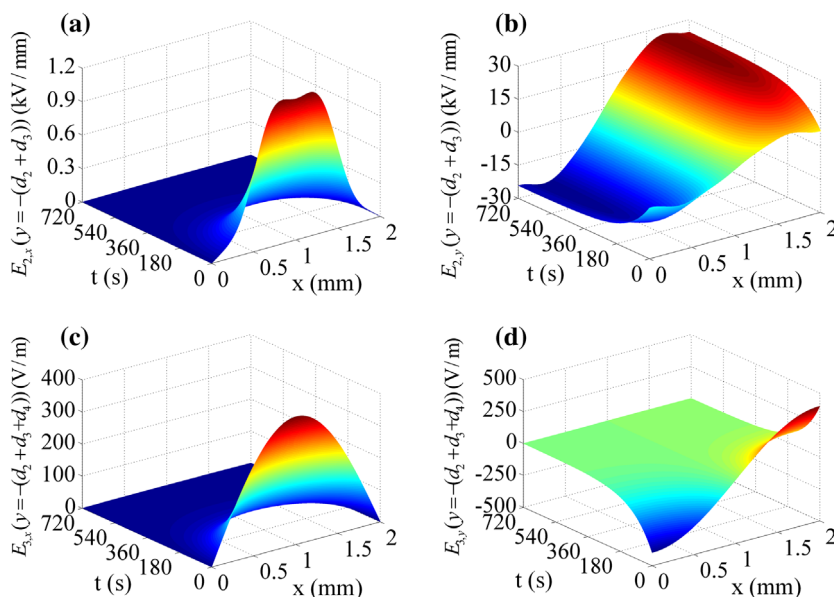


Figure 8. The step response of the electric field components as a function of time (t) and distance (x) along the boundary $y = -(d_2 + d_3)$ in region 2 [(a) and (b)] and $y = -(d_2 + d_3 + d_4)$ in region 3 [(c) and (d)] (PVDF plate).

phase due to the incomplete contact between the electrode panel and the substrate plate. As the adhesion force increases with time, the thickness of the air layer decreases due to more complete contact between the electrode panel and the substrate plate. Therefore, the

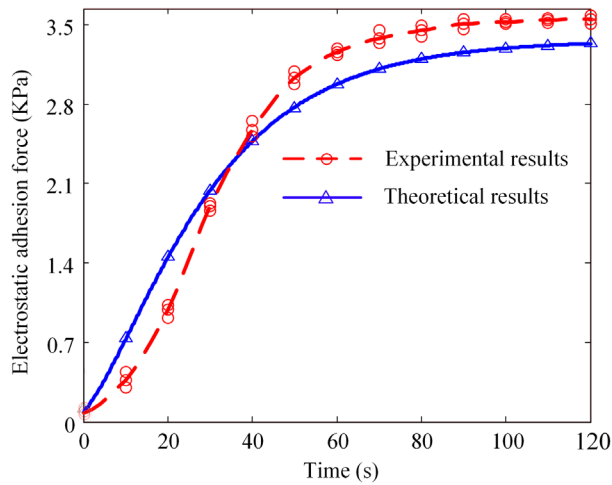


Figure 9. Time histories of the electrostatic adhesion force exerted on the glass plate. Theoretical results (---) and experimental results (—).

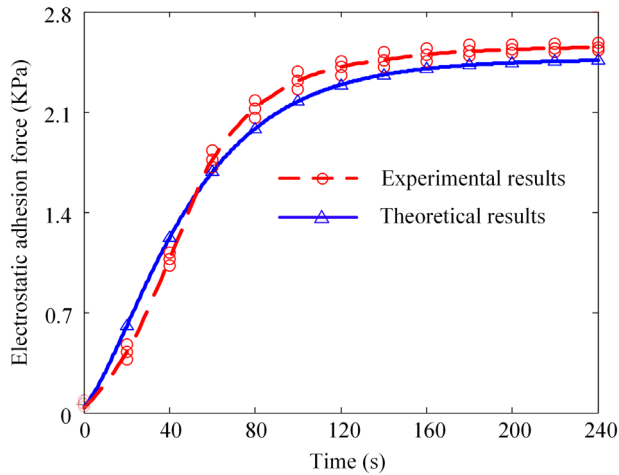


Figure 10. Time histories of the electrostatic adhesion force exerted on the wood plate. Theoretical results (---) and experimental results (—).

experimental values are larger than the theoretical values in the later phase. In addition, the steady-state values of the adhesion forces and the time required for the adhesion forces to reach steady-state values are different on three substrate plates. This is associated with the different conductivities of the substrate plates.

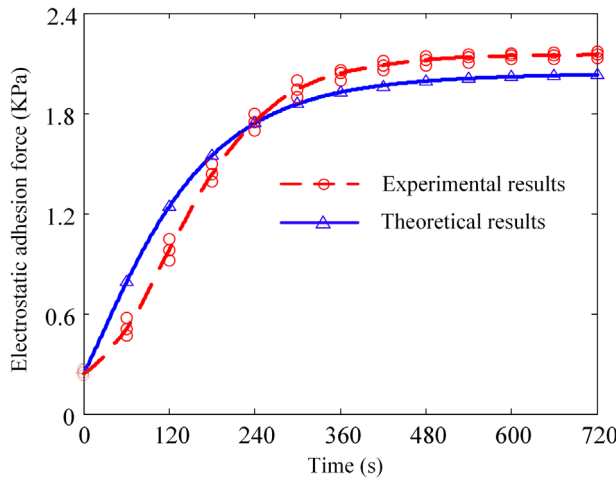


Figure 11. Time histories of the electrostatic adhesion force exerted on the PVDF plate. Theoretical results (---) and experimental results (—).

4. Discussion

4.1. Approximation of the interelectrode potential

The potential distribution on the entire electrode plane, bounded by the plane $y = 0$, represents one of the boundary conditions required to determine the field distribution in sub-area 1. Nevertheless, we apply known voltages only to the electrodes in practical electrode panel while the potential distributions between the electrodes are unknown. In the physical model given above, for clarity and convenience, we take the first-order Taylor series approximation, assuming that the potential varies linearly with distance in the electrode gaps.

Since the electrodes are placed in a homogeneous dielectric medium (the top and bottom surface of the copper electrodes are both covered by a polyimide film), the field in the direction normal to the electrode plane is zero within the electrode gaps. This additional constraint for the electrical field configuration can be used to determine the potentials in the electrode gaps. The approach is as follows. First, the electrical potential in each interelectrode gap is expanded as a Taylor series with respect to the distance from the electrode gap centre with undetermined polynomial coefficients. Then, the expressions for the electrical potential and electric field component everywhere in terms of the undetermined coefficients can be obtained through symbolic calculation. Finally, values for these coefficients are determined by applying the field constraint condition, so that the field results are self-consistent.

The Taylor expansion of the electrical potentials in the electrode gaps is given as follows (even terms disappear due to the electrode symmetry):

$$\phi(x, 0, t) = \frac{V_p(t) + V_n(t)}{2} + \frac{V_n(t) - V_p(t)}{2} \sum_{m=0}^{\infty} \alpha_{2m+1} (x - p/2)^{2m+1}, \quad (29)$$

where $w \leq x \leq p - w$, and the polynomial coefficients α_{2m+1} ($m = 0, 1, 2, \dots$) satisfy:

$$\sum_{m=0}^{\infty} \alpha_{2m+1} (p/2 - w)^{2m+1} = 1. \quad (30)$$

We derive the analytical expressions for the field components and electrostatic adhesion force by substituting $\phi(x, 0, t)$ in terms of the undetermined polynomial coefficients α_{2m+1} into the derivation process in Section 2, most conveniently by using symbolic manipulation by computer. The polynomial coefficients α_{2m+1} can then be determined from the constraint:

$$E_y(x, 0, t) = 0 \quad w \leq x \leq p - w. \quad (31)$$

Practically, a finite number of polynomial terms is taken as an approximation, and an optimization function for determining the coefficients is then used to minimize the error resulting from the finite number of terms:

$$\min_{\alpha_1, \alpha_1, \dots, \alpha_{2m+1}} \left\{ \int_w^{p-w} E_y^2(x, 0, t) dy \right\}. \quad (32)$$

Evidently, the optimization procedure results in the smallest magnitude of E_y values in such a way that these magnitudes alternate about zero. Generally, a third or five order approximation for the potential in the interelectrode gap is adopted by considering the model accuracy and complexity of computation at the same time.

4.2. Truncation of series expansions of the field components

From a computational perspective, the series expansion of the field components, which involve summations over an infinite number of terms, needs to be truncated. The total number (n_{total}) of the summation terms required to sufficiently model the field dynamics and achieve reasonable model accuracy can be determined by identifying the dominant poles of the second order transfer functions for the field components given by Equation (23). Figure 12 depicts the poles $p_1(n)$ and $p_2(n)$ as a function of the summation index n . $p_1(n)$ and $p_2(n)$ reflect the different speeds at which charges accumulate on the boundary $y = -d_2$ and on the boundary $y = -(d_2 + d_3)$. Since the bulk conductivity of the polyimide film is much smaller than that of the glass panel, charges accumulation occurs mainly and is much quicker at the boundary $y = -(d_2 + d_3)$. The dynamic properties of the field and adhesion force are mainly reflected by $p_2(n)$ in the actual application. As the integer n varies from 1 to 31, $p_2(n)$ decreases from -0.052 to -0.242 . For higher values of n , $p_2(n)$ does

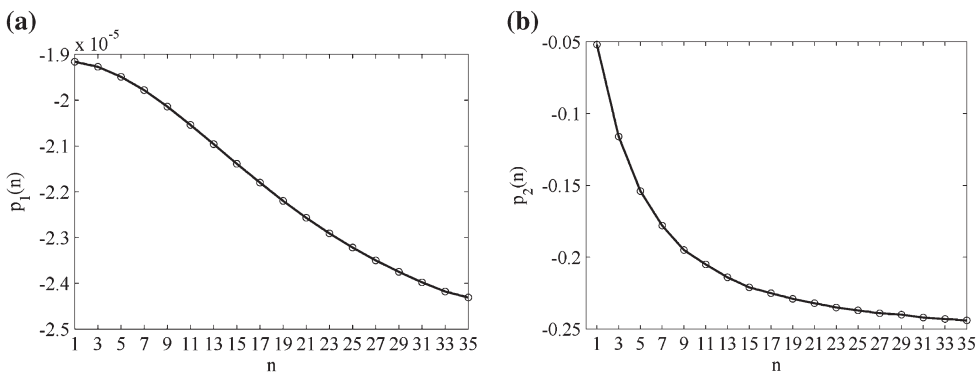


Figure 12. Dependency of the transfer function poles $p_1(n)$ [(a)] and $p_2(n)$ [(b)] on summation index n .

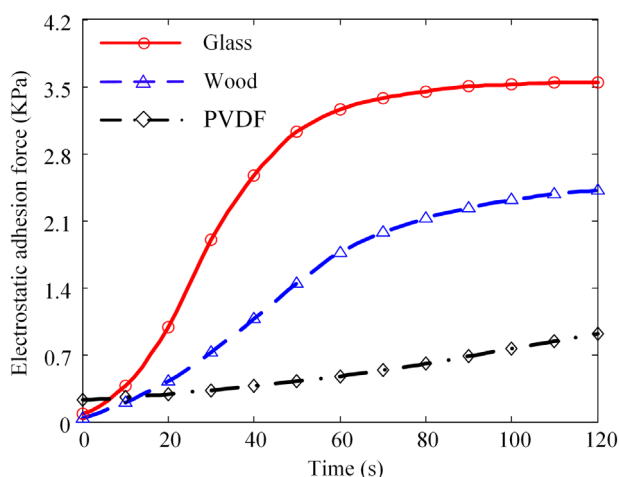


Figure 13. Dynamic variation of the electrostatic adhesion forces on three substrate plates.

not show any signs of a steady decrease but instead levels off at around -0.25 . Meanwhile, we notice that the magnitude of field components decrease sharply as the integer value of n increases. Based on the above considerations, the choice of $n_{\text{total}} = 31$ is verified to lead to a rapid convergence of the sum, and the dynamic properties of field and adhesion force can also be demonstrated well.

4.3. Difference of response speeds on three substrate plates

In order to deeply analyse the dynamic properties of electrostatic adhesion on three substrate plates of different materials, the difference of response speeds of the electrode panel on the substrate plates was plotted in Figure 13. The dynamic response speed on the glass plate is the fastest while the slowest response speed occurred on the PVDF plate. Although the initial value of adhesion force on the PVDF plate is larger than that on the glass plate, the maximum magnitude of the adhesion force on the glass plate is larger than that of on the PVDF plate after some time as the step voltages applied. The results indicate that the dynamic property of electrostatic adhesion is a very important issue since the steady-state value of the electrostatic adhesion force is much larger than the initial value.

5. Conclusion

This paper has proposed a theoretical model to analyse the dynamic properties of the electric field and electrostatic adhesion force in a typical electrostatic adhesion system. A dynamic relation that includes a time-delay function between the electrostatic adhesion force and the applied voltage is obtained. The amount of time required for the force to build-up mainly depends on the relative permittivity and the resistivity of the materials. Experimental results from the three different substrate plates show relatively good agreement with the theoretical model. The dynamic properties of the electrostatic adhesion applied to dielectric materials should be seriously considered to keep and maintain adhesion stability.

Although the model proposed in this paper is based on coplanar interdigital electrodes, it can be easily extended to other geometries, such as concentric circles, square spiral and so on with some tweaking. Additionally, the paper makes the assumption that the substrate thickness is much greater than that of the insulating base layer and the air layer, which applies to most cases. However, regarding adhesion to thin films like mylar sheet, paper sheet and so on, the model proposed in this paper will result in certain deviation. The model proposed in this paper can be applied to many electrostatic adhesion problems, especially problems where interdigital electrodes are utilized to generate electric field and electrostatic adhesion force, such as the electrostatic chuck and electrostatic suspension system used in industry areas, and wall-climbing robots using electrostatic adhesion force. The outcome of this work can provide support for theoretical guidelines and system optimization for these electrostatic applications.

Disclosure statement

No potential conflict of interest was reported by the authors.

Funding

This work was supported by the National Natural Science Foundation of China [grant number 51505044]; the National Key Technology R&D Program [grant number 2015BAF17B02]; and the Basic and Advanced Research Project of Chongqing [grant number cstc2015jcyjA70002].

References

- [1] Castle GSP. The evolving field of electrostatics. *Inst Phys Conf Ser.* **1991**;108:1–12.
- [2] Yatsuzuka K, Hatakeyama F, Asano K, et al. Fundamental characteristics of electrostatic wafer chuck with insulating sealant. *IEEE Trans Ind Appl.* **2000**;36:510–516.
- [3] Asano K, Hatakeyama F, Yatsuzuka K. Fundamental study of an electrostatic chuck for silicon wafer handling. *IEEE Trans Ind Appl.* **2002**;38:840–845.
- [4] Jeon JU, Higuchi T. Electrostatic suspension of dielectrics. *IEEE Trans Ind Electron.* **1998**;45:938–946.
- [5] Ju J, Yih TC, Higuchi T, et al. Direct electrostatic levitation and propulsion of silicon wafer handling. *IEEE Trans Ind Appl.* **1998**;34:975–984.
- [6] Jeon JU, Park K, Higuchi T. Contactless suspension and transportation of glass panels by electrostatic forces. *Sens Actuators, A.* **2007**;134:565–574.
- [7] Green NG, Ramos A, Morgan H. Numerical solution of the dielectrophoretic and travelling wave forces for interdigitated electrode arrays using the finite element method. *J Electrostat.* **2002**;56:235–254.
- [8] Wang XJ, Wang XB, Becker FF, et al. A theoretical method of electrical field analysis for dielectrophoretic electrode arrays using Green's theorem. *J Phys D: Appl Phys.* **1996**;29:1649–1660.
- [9] Garcia M, Clague D. The 2D electric field above a planar sequence of independent strip electrodes. *J Phys D: Appl Phys.* **2000**;33:1747–1755.
- [10] Morgan H, Izquierdo AG, Bakewell D, et al. The dielectrophoretic and travelling wave forces generated by interdigitated electrode arrays: analytical solution using Fourier series. *J Phys D Appl Phys.* **2001**;34:1553–1561.
- [11] Yamamoto A, Nakashima T, Higuchi T. Wall climbing mechanisms using electrostatic attraction generated by flexible electrodes. *Int Symp Micro-Nano Mechatron Human Sci.* **2007**;1:389–394.

- [12] Prahlad H, Pelrine R, Stanford S, et al. Electroadhesive robots – wall climbing robots enabled by a novel, robust, and electrically controllable adhesion technology. IEEE International Conference on Robotics and Automation; 2008 May 19–23; Pasadena, CA, USA.
- [13] Liu R, Chen R, Shen H, et al. Wall climbing robot using electrostatic adhesion force generated by flexible interdigital electrodes. *Int J Adv Robot Syst.* **2013**;10:1–9.
- [14] Guo JL, Justham L, Jackson M, et al. A concept selection method for designing climbing robots. *Key Eng Mater.* **2015**;649:22–29.
- [15] Krape RP. Applications study of electroadhesive devices. NASA report CR-1211, Chrysler Corp. Space Division; **1968**.
- [16] Kalkowski G, Risse S, Harnisch G, et al. Electrostatic chucks for lithography applications. *Microelectron Eng.* **2001**;57–58:219–222.
- [17] Zhang ZW. Modeling and analysis of electrostatic force for robot handling of fabric materials. *IEEE/ASME Trans Mechatron.* **1999**;4:39–49.
- [18] Zhang ZW, Chestney JA, Sarhadi M. Characterizing an electrostatic gripping device for the automated handling of non-rigid materials. *P I Mech Eng B-J Eng.* **2001**;215:21–36.
- [19] Guo JL, Taylor M, Bamber T, et al. Investigation of relationship between interfacial electroadhesive force and surface texture. *J Phys D: Appl Phys.* **2016**;49:035303.
- [20] Chen R, Liu R, Shen H. Modelling and analysis of electric field and electrostatic adhesion force generated by interdigital electrodes for wall climbing robots. IEEE/RSJ International Conference on Intelligent Robots and Systems; 2013 November 3–7; Tokyo, Japan.
- [21] Haus HA, Melcher JR. Electromagnetic fields and energy. Upper Saddle River, NJ: Prentice Hall; **1989**.
- [22] Melcher R. Continuum electromechanics. Cambridge, MA: MIT Press; **1981**.

Appendix 1. Solution to the Laplace equation

The Laplace equation was solved by symbolic computations of the MATLAB software package. The analytical solutions of the Laplace transforms of the eight unknown time-varying coefficients were given by:

$$K^1(s) = K^2(s) = K^3(s) = \frac{1}{2} \left[V_p(s) + V_n(s) \right],$$

$$L_n^1(s) = V_{\nabla}(s)\gamma(n) \frac{a_{2,L_1}(n)s^2 + a_{1,L_1}(n)s + a_{0,L_1}(n)}{b_2(n)s^2 + b_1(n)s + b_0(n)},$$

$$L_n^2(s) = V_{\nabla}(s)\gamma(n) \frac{a_{2,L_2}(n)s^2 + a_{1,L_2}(n)s + a_{0,L_2}(n)}{b_2(n)s^2 + b_1(n)s + b_0(n)},$$

$$L_n^3(s) = V_{\nabla}(s)\gamma(n) \frac{a_{2,L_3}(n)s^2 + a_{1,L_3}(n)s}{b_2(n)s^2 + b_1(n)s + b_0(n)},$$

$$M_n^1(s) = V_{\nabla}(s)\gamma(n),$$

$$M_n^2(s) = V_{\nabla}(s)\gamma(n) \frac{a_{2,M_2}(n)s^2 + a_{1,M_2}(n)s + a_{0,M_2}(n)}{b_2(n)s^2 + b_1(n)s + b_0(n)},$$

where

$$V_{\nabla}(s) = V_p(s) - V_n(s),$$

$$\gamma(n) = \begin{cases} 0 & n = \text{even} \\ \frac{4 \cos(n\pi w/p)}{n^2 \pi^2 (1-2w/p)} & n = \text{odd} \end{cases}.$$

The numerator polynomial coefficients, which are functions of the summation index n , are defined as:

$$a_{2,L_1}(n) = \varepsilon_0^2 \cosh\left(\frac{n\pi d_2}{p}\right) \sinh\left(\frac{n\pi d_3}{p}\right) + \varepsilon_0 \varepsilon_p \cosh\left(\frac{n\pi d_3}{p}\right) \sinh\left(\frac{n\pi d_2}{p}\right) + \varepsilon_d \varepsilon_p \sinh\left(\frac{n\pi d_3}{p}\right) \sinh\left(\frac{n\pi d_2}{p}\right) + \varepsilon_0 \varepsilon_d \cosh\left(\frac{n\pi d_3}{p}\right) \cosh\left(\frac{n\pi d_2}{p}\right),$$

$$a_{1,L_1}(n) = \varepsilon_0 \sigma_d \cosh\left(\frac{n\pi d_2}{p}\right) \cosh\left(\frac{n\pi d_3}{p}\right) + \varepsilon_0 \sigma_p \cosh\left(\frac{n\pi d_3}{p}\right) \sinh\left(\frac{n\pi d_2}{p}\right) + \varepsilon_d \sigma_p \sinh\left(\frac{n\pi d_3}{p}\right) \sinh\left(\frac{n\pi d_2}{p}\right) + \varepsilon_p \sigma_d \sinh\left(\frac{n\pi d_3}{p}\right) \sinh\left(\frac{n\pi d_2}{p}\right),$$

$$a_{0,L_1}(n) = \sigma_d \sigma_p \sinh\left(\frac{n\pi d_2}{p}\right) \sinh\left(\frac{n\pi d_3}{p}\right),$$

$$a_{2,L_2}(n) = \varepsilon_d \varepsilon_p \cosh\left[\frac{n\pi(d_2 + d_3)}{p}\right] + \varepsilon_0 \varepsilon_p \sinh\left[\frac{n\pi(d_2 + d_3)}{p}\right],$$

$$a_{1,L_2}(n) = \varepsilon_d \sigma_p \cosh\left[\frac{n\pi(d_2 + d_3)}{p}\right] + \varepsilon_0 \sigma_p \sinh\left[\frac{n\pi(d_2 + d_3)}{p}\right] + \varepsilon_p \sigma_d \cosh\left[\frac{n\pi(d_2 + d_3)}{p}\right],$$

$$a_{0,L_2}(n) = \sigma_d \sigma_p \cosh\left[\frac{n\pi(d_2 + d_3)}{p}\right],$$

$$a_{2,L_3}(n) = \varepsilon_0 \varepsilon_p \exp\left[\frac{n\pi(d_2 + d_3)}{p}\right],$$

$$a_{1,L_3}(n) = \varepsilon_0 \sigma_p \exp\left[\frac{n\pi(d_2 + d_3)}{p}\right],$$

$$a_{2,M_2}(n) = \varepsilon_d \varepsilon_p \sinh\left[\frac{n\pi(d_2 + d_3)}{p}\right] + \varepsilon_0 \varepsilon_p \cosh\left[\frac{n\pi(d_2 + d_3)}{p}\right],$$

$$a_{1,M_2}(n) = \varepsilon_d \sigma_p \sinh\left[\frac{n\pi(d_2 + d_3)}{p}\right] + \varepsilon_0 \sigma_p \cosh\left[\frac{n\pi(d_2 + d_3)}{p}\right] + \varepsilon_p \sigma_d \sinh\left[\frac{n\pi(d_2 + d_3)}{p}\right],$$

$$a_{0,M_2}(n) = \sigma_d \sigma_p \sinh \left[\frac{n\pi(d_2 + d_3)}{p} \right].$$

Finally, the denominator polynomial coefficients are given by:

$$b_2(n) = \varepsilon_0^2 \sinh \left(\frac{n\pi d_2}{p} \right) \sinh \left(\frac{n\pi d_3}{p} \right) + \varepsilon_0 \varepsilon_p \cosh \left(\frac{n\pi d_3}{p} \right) \cosh \left(\frac{n\pi d_2}{p} \right) + \varepsilon_d \varepsilon_p \sinh \left(\frac{n\pi d_3}{p} \right) \cosh \left(\frac{n\pi d_2}{p} \right) \\ + \varepsilon_0 \varepsilon_d \cosh \left(\frac{n\pi d_3}{p} \right) \sinh \left(\frac{n\pi d_2}{p} \right),$$

$$b_1(n) = \varepsilon_0 \sigma_d \sinh \left(\frac{n\pi d_2}{p} \right) \cosh \left(\frac{n\pi d_3}{p} \right) + \varepsilon_0 \sigma_p \cosh \left(\frac{n\pi d_3}{p} \right) \cosh \left(\frac{n\pi d_2}{p} \right) + \varepsilon_d \sigma_p \sinh \left(\frac{n\pi d_3}{p} \right) \cosh \left(\frac{n\pi d_2}{p} \right) \\ + \varepsilon_p \sigma_d \sinh \left(\frac{n\pi d_3}{p} \right) \cosh \left(\frac{n\pi d_2}{p} \right),$$

$$b_0(n) = \sigma_p \sigma_d \cosh \left(\frac{n\pi d_2}{p} \right) \sinh \left(\frac{n\pi d_3}{p} \right).$$